Hydrophobic Residues Promote Interfacial Activation of Candida Rugosa Lipase: A Study of Rotational Dynamics

Ava Waggett

A thesis
submitted in partial fulfillment of the
requirements for the degree of

Master of Science in Chemical Engineering

University of Washington
2024

Committee:
Jim Pfaendtner
Christopher Mundy

Program Authorized to Offer Degree:
Chemical Engineering

University of Washington

Abstract

Hydrophobic Residues Promote Interfacial Activation of Candida Rugosa Lipase: A Study of Rotational Dynamics

Ava Waggett

Chair of the Supervisory Committee:
Jim Pfaendtner
Chemical Engineering

Microbial lipases constitute a class of biocatalysts with the ability to cleave ester linkages of long-chain triglycerides, a property which makes them particularly attractive for industrial applications ranging from food processing to pharmaceutical preparation. *Candida rugosa* lipase (CRL) is among the enzymes most frequently used in biotransformation. A notable feature of CRL is its propensity for interfacial activation, exhibiting elevated catalytic rates when acting at the interface between aqueous and hydrophobic phases. This phenomenon can be understood in the context of the enzyme's hydrophobic substrate and the presence of a mobile lid domain. To advance our understanding of interfacial activation, we explore the dynamics of CRL rotation at the octane-water interface in this work. To do so, we employ Molecular Dynamics to evaluate the free energy of rotation at the interface, identifying a global minimum at the point of lid alignment to the interface that coincides with and is further stabilized by lid opening. Additionally, we investigate the role of leucine residues outside of the lid domain as they serve to instigate rotation of the lid towards the interface. These findings serve to further elucidate the mechanism of CRL activation at the oil-water interface and point towards a holistic effect of rotation and lid opening that is mediated by both lid and non-lid surface residues.

Introduction

Candida rugosa lipase (CRL) is a biocatalyst that has found widespread use in industrial hydrolytic applications including polymer synthesis, food processing, biodiesel production, and pharmaceutical preparation[1–5]. While the value of CRL as a biocatalyst derives from its high regio-, chemo-, and enantioselectivity, industrial applications are limited by the sensitivity of the enzyme to the solvent environment[6–8]. In particular, the activity of lipases, as with CRL, is typically dependent on interfacial activation as it demonstrates marked activity increase at the oil-water interface[9]. This can be understood as a coupling of the water-soluble enzyme and its water-insoluble substrates, typically triacylglycerol[9]. In response to this challenge, several immobilization methods have been developed to elicit and retain enzyme activation, including covalent binding, cross-linking, and encapsulation[10–12]. Notably, these methods can make use of hydrophobic supports to achieve activity increases akin to interfacial activation.

The phenomenon of interfacial activation has been elucidated by the discovery of a common structural motif among lipases: a mobile lid domain. The lid domain, also referred to as a flap, differentiates the open (active) and closed (inactive) states of the enzyme. In its active state, the lid domain of CRL hinges open to expose an L-shaped hydrophobic intramolecular tunnel containing the active site: the catalytic triad consisting of residues Ser209, Asp187, His224 and the oxyanion hole (Gly124 and Ala210)[13]. In its inactive state, the helical lid domain occludes the active site, preventing solvent and substrate access. The lid domain itself is amphipathic: in its closed state, the hydrophilic side faces the solvent whereas the hydrophobic side faces the interior of the protein, including the aromatic and aliphatic residues at the base of the intramolecular tunnel[13–15]. The flap is anchored by a disulfide bond involving Cys60-Cys97 and a salt bridge involving Glu95-Arg37[16]. The lid domain is identified as residues 60-97, bookended by the disulfide bridge.

Not simply a matter of rigid rotation, transition between states is accompanied by rearrangement of the flap secondary structure and isomerization of the Pro92 peptide bond[16]. Additionally, hydrophobic patches in the vicinity of the lid domain (e.g., residues 439 to 459) are known to play a role in lid opening[16]. In comparing lid closed and open crystal structures, the same hydrophobic patch transitions from intramolecular hydrophobic interactions with the lid domain (closed) to intermolecular hydrophobic interactions (open) with the same lid residues of the symmetry-related molecule, hinting at the role of the hydrophobic layer in stabilizing the lid open state[16]. To clarify the role of hydrophobic surface patches on CRL, in this work we dive deeper into the association of hydrophobic residues with the oil-water interface and highlight their importance for aligning the lid with the interface prior to opening.

When produced by nonsporogenic yeast, Candida rugosa, enzyme CRL is typically harvested as a mixture of isozymes, each exhibiting unique catalytic properties[17]. This study focuses on the CRL1 isoform as it the most widely used isozyme, has been structurally characterized in both its open and closed states via x-ray crystallography[13,16], and is known to exhibit interfacial activation[17]. Importantly, the activation of CRL1 has been demonstrated to be the rate-limiting step in catalysis where only the existence of a highly hydrophobic interface was able to shift the equilibrium towards the open conformation of the lipase[18].

Within this context, myriad experimental and computational studies have sought to explore the phenomenon of interfacial activation under varying solvent, pH, temperature, and support conditions[6,7,19]. Immobilization protocols have been explored to impart varying degrees of enzyme rigidity and manipulate the microenvironment so as to shift equilibrium dynamics towards the open state[10,12,20,21]. Beyond immobilization methods, the activity and selectivity of lipase CRL has been explored via mutagenesis. Previous structure-function relationships have largely consisted of either swapping regions of isoforms to create chimeric lipases or site-directed mutagenesis studies, with specific emphasis on residues within the lid domain and hydrophobic tunnel[22–25]. These experimental studies have likewise been joined by Molecular Dynamics studies of lipases concerning the effect of mutations on interfacial activation[26–30].

Whereas previous computational approaches have emphasized the role of lid domain and active site residues as determinant of substrate specificity and enzyme activity, this work explores the impact of residues outside the lid domain on preferential adoption of the lid open state. More specifically, we probe the role of leucine residues which constitute a hydrophobic patch vicinal to the lid domain through site-directed mutagenesis of select residues to glycine. Classical simulations and Umbrella Sampling are employed to explore and define the rotational free energy landscape for native and mutant enzymes acting at the octane-water interface. In the absence of 6 hydrophobic leucine residues, we demonstrate a barrier to rotation that precludes lid opening on the time scale of 1 microsecond. In this way, we demonstrate how mutagenesis disrupts hydrophobic regions of the enzyme surface that in the native state serve to facilitate rotation of the lid towards the oil phase. This work serves to demonstrate the holistic effect of hydrophobic surface patches outside and within the lid domain which work in series to accomplish enzyme rotation and lid opening at the oil-water interface. To our knowledge, this is the first study to explore the impact of hydrophobic residues neighboring the lid domain on the rotational dynamics and subsequent conformational dynamics of the lid.

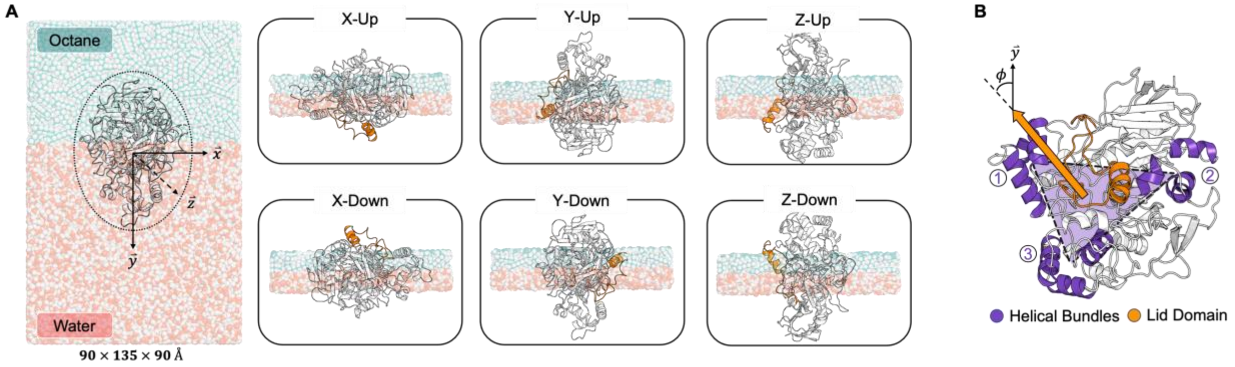

Figure 1. Initialization. (a) The equilibrated structure for enzyme CRL in water was extracted and fit to an ellipsoid, defining three principal axes for the enzyme: x, y, and z. For each of the six initial states of the enzyme at the octane-water interface, each principal axis was oriented orthogonal to the interface dimension (y) and either pointing in the direction of the octane phase (up) or the water phase (down). Structure X-Up orients the lid domain (orange) such that it is entirely solvated by the aqueous phase; structure X-Down, entirely in the octane phase. The remaining structures orient the lid at the interface. (b) An internal vector is defined to facilitate calculation of the enzyme orientation relative to the interface. Specifically, the centers of mass of three bundles of α-helices are used to establish a stable plane within the enzyme. The normal to this plane is used to calculate the angle to the interfacial dimension (y), referred to as ϕ.

Theoretical Methods

Classical MD Simulations. All Molecular Dynamics simulations were performed using the PMEMD engine of Amber 20[31,32] with full periodic boundary conditions. The necessary forcefield parameters for protein, water, octane, and ions were obtained from FF19SB[33], OPC3 water model[34], General Amber Force Field (gaff)[35], and Li-Merz 6-12 OPC3 ion parameters[36], respectively. Octane molecules were parametrized with the General Amber force field, with partial charges computed via the residual electrostatic potential (REsP)[37] fitting method in antechamber, using the Hartree-Fock level with the 6-31G* basis set in Gaussian 16[38]. The SHAKE[39] algorithm was applied to constrain bonds involving hydrogen atoms while the SETTLE[40] algorithm was applied to constrain water molecules. In addition, Hydrogen Mass Repartitioning[41] was employed with a mass increase to 3.024 Daltons per hydrogen atom, affording the use of a 4 fs time step for all simulations. A cutoff distance of 8 Å was chosen for evaluation of nonbonded interactions including electrostatic and van der Waals forces. Long range interactions were computed according to the Particle Mesh Ewald summation method[42].

All classical simulations followed the same minimization and equilibration protocol as follows. An initial energy minimization was performed for all systems consisting of a short steepest descent energy minimization followed by a maximum of 2,500 steps of conjugate gradient minimization. Next, the temperature was increased in stages up to 300K over 500 ps using the Bussi thermostat[43] (a stochastic version of the Berendsen thermostat, τ=1) in the NVT ensemble. The system was pressurized to 1 atm at 300 K for 1 ns using the Berendsen barostat[44] (τ=1) and Bussi thermostat in the NPT ensemble. To capture fluctuations more accurately in the NPT ensemble, the Monte Carlo barostat[45] (a stochastic version of the Berendsen barostat) was used to control pressure in all production runs.

Initial structures for CRL in the closed (pdb: 1TRH)[16] and open (pdb: 1CRL)[13] lid states were obtained from the Protein Data Bank. All simulations originate from the closed lid structure with the open lid structure used solely as a reference state for analysis. The online MD preparation software H++[46] was used to predict the protonation state of ionizable groups of CRL at pH 7, yielding a net charge of -11. All systems were neutralized with sodium ions. 2 Disulfide bonds were defined between cystine residues 60 and 97 and residues 268 and 277. Prior to constructing the oil-water interface, CRL was initially equilibrated in water according to the protocol outlined above.

System Initialization. After initial equilibration, the enzyme was extracted, and software Visual Molecular Dynamics[47] was used to align the three principal axes of the enzyme to the x, y, and z directions. Next, initial configurations for the enzyme-interface systems were assembled using

PACKMOL[48], consisting of CRL, 1,376 octane molecules, 20,832 water molecules, and 11 sodium ions in a 9x13.5x9 nm box. The orientation of the enzyme was systematically adjusted to sample rotation at the interface from varying initial states: in each configuration, the enzyme was centered at the oil-water interface with one of the 3 principal axes oriented orthogonal to the interface and pointing towards either the octane or water phases. This resulted in 6 unique configurations, hereafter referred to as X-Up, X-Down, Y-Up, Y-Down, Z-Up, and Z-Down. The starting orientations are shown in Figure 1 panel A with the lid domain highlighted in orange. Classical simulations were run for a total of 350 ns unless otherwise indicated. Two additional trials for the X-Up configuration were run based on the complex rotational landscape demonstrated by the initial trial.

To monitor the enzyme's orientation relative to the interface, we constructed a collective variable (CV) based on the relative positions of three helical bundles of α-helices within the enzyme. The center of mass of each helical bundle was used to construct a plane internal to the protein, lying below the lid domain. The protein orientation was then defined as the normal to the internal plane. We define ϕ, the angle of the enzyme relative to the interface, as the angle between the protein vector and the interface normal, pointing in the direction of the octane phase (i.e., the y-unit vector) (Figure 1).

Based on subsequent analyses of relevant surface amino acids, 6 leucine residues were mutated to glycine to eliminate hydrophobic interactions between the sidechains and the octane phase. Residues were directly mutated in the text of the pdb, retaining only backbone atoms. Then the structure of the mutated side chains was completed by Amber's tleap module. The stability of the enzyme backbone following mutation was verified for all trials of unbiased mutant simulations (Figure S14).

Umbrella Sampling. Two sets of Umbrella Sampling (US) simulations were performed to evaluate the free energy of rotation for CRL at the oil-water interface subject to lid domain rearrangement and surface residue mutation. In both cases, a set of 79 windows were equally distributed every 0.035 rad (2°) between $\phi = 0.35$ and $\phi = 2.97$ rad ($\phi = 20°$ and $\phi = 170°$) to the interface. For the native protein, initial configurations for each window were selected from unbiased trials of X-Up. For the mutant protein, unbiased frames spanning the reaction coordinate were obtained following steering, as addressed in the next section. US simulations were conducted with the Amber 20 MD engine patched to the PLUMED library (version 2.7.3)[49–51] for restraint handling. A harmonic angle restraint of $5{,}000\ \frac{\mathrm{kcal}}{\mathrm{mol \cdot rad}}$ was applied for initial runs of 15 ns for all windows. For the last 10 ns of simulation (reserving 5 ns for equilibration) the number of lid residues in contact with the octane phase (within 4 Å) was evaluated. Based on the results of the calculation, the windows were split into two categories: interfacial (the lid domain is in contact with octane) and aqueous (the lid domain is not in contact with octane). To minimize computational expense and with consideration of the additional time required for lid domain rearrangement at the interface, the equilibration time for the two categories of windows was extended nonuniformly: aqueous windows were extended up to 25 ns of equilibration whereas interfacial windows were extended up to 40 ns of equilibration. All production frames included 10 ns of simulation time. The effect of varying equilibration time is shown in Figure S12 and demonstrates convergence in the aqueous windows at 25 ns of equilibration and in the interfacial windows at 35 ns of equilibration. The free energy surface was constructed by reweighting the observed configurations according to the Weighted Histogram Analysis Method (WHAM)[52]. Error analysis was performed via Monte Carlo bootstrapping.

Steered MD Simulations. Given the lack of rotation beyond $\phi = 2$ rad in unbiased simulations of mutant enzymes, we chose to steer CRL between angles 2.1 and 1.3 rad with a restraint of $5{,}000\ \frac{\mathrm{kcal}}{\mathrm{mol \cdot rad}}$ and at a pulling rate of $0.018\ \frac{\mathrm{rad}}{\mathrm{ns}}$. The stability of the enzyme during steering was verified (Figure S17). Structures along the steering trajectory were extracted and used as initial frames for unbiased simulations and run for 100 ns. These trials either demonstrated rotation back to $\phi \approx 2$ rad or continued rotation to $\phi \approx 0.4$ rad, as was observed in the native enzyme simulations, depending on the angle from steering at which the run was initialized. In turn, the resulting unbiased frames that spanned the reaction coordinate ($\phi = 0.35$ to $\phi = 2.97$ rad) were used as initial frames for US (Figure S17).

Simulation Analysis. Trajectories were analyzed using a combination of Amber 20 CPPTRAJ module[32], PLUMED library (version 2.7.3), MDAnalysis python library[53,54], and MDTraj python library[55]. All molecular visualizations were generated using Pymol[56].

Results and Discussion

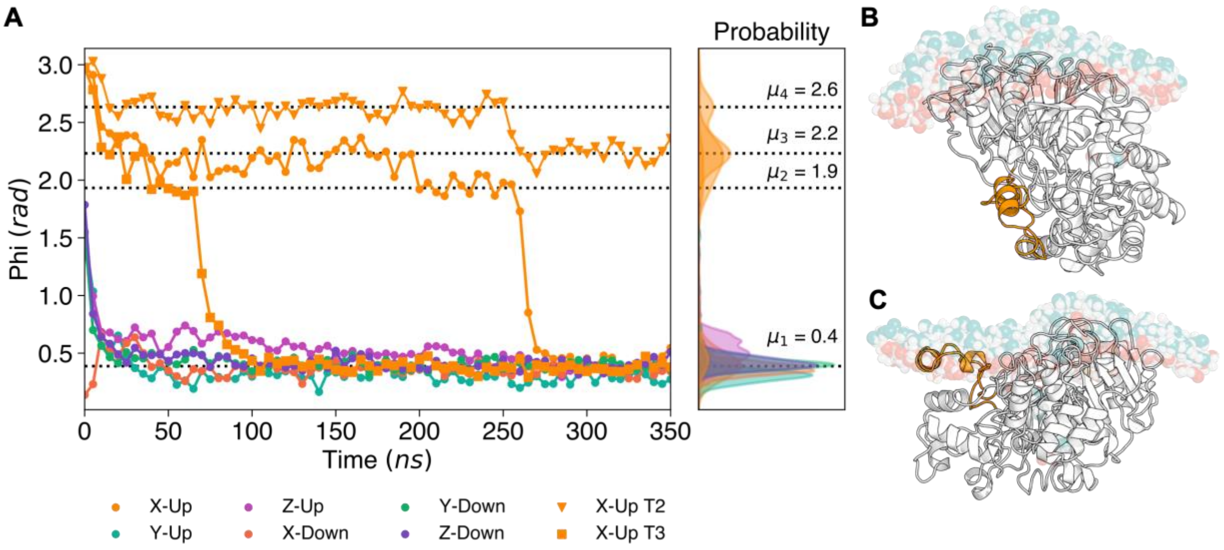

Figure 2. Simulation predictions of CRL orientation at the octane-water interface. (a) The time series data monitors the value of ϕ (CV defining enzyme orientation relative to the interface). Each distinct initial orientation is differentiated by color. Data is plotted every 5 ns for clarity. Additional trials beginning from the X-Up state (orange) are differentiated by marker shape. All trials show rotation towards $\phi \approx 0.4$ rad within 350 ns, apart from X-Up trial 2. Probability density plots are shown to highlight regions of stability. All data within the first 350 ns of simulation was fit to a sum of four gaussians, resulting in 4 mean values representing the centers of each distribution that are marked by dotted lines and text. Structures corresponding to semi-stable states at $\phi \approx 2.2$ rad (b) and $\phi \approx 0.4$ rad (c) are shown along with octane (blue) and water (red) molecules within 1 nm of the interface. The lid domain is contrasted in orange with the rest of the protein in white.

Native CRL exhibits consistent rotation towards the oil-water interface accompanied by lid opening. We initially sought to evaluate the tendency for CRL to rotate at the oil-water interface beginning from a diversity of initial states (X-Up, X-Down, Y-Up, Y-Down, Z-Up, and Z-Down). The starting orientation of the enzyme relative to the interface is highlighted in Figure 1. Notably, the lid domain begins immersed in the octane phase in the X-Down state, immersed in aqueous phase in the X-Up state, and contacting both phases for all other initial states. Figure 2 demonstrates the orientation of the enzyme, as defined by the enzyme-interface vector (ϕ), over the course of 350 ns of simulation per trial. A root mean squared deviation (RMSD) for all α-carbons contained within the helical domains of the CV was evaluated for all trials. Results in Figure S1 demonstrate insignificant rearrangement, validating the stability of the CV during enzyme rotation and lid domain opening. In response to the complex rotational landscape exhibited by the X-Up configuration, we elected to run two additional trials starting from the same initial state (X-Up T2 and X-Up T3). All trials show rotation to a final angle of $\phi \approx 0.4$ rad. (X-Up T2 shows rotation to $\phi = 0.4$ rad after approximately 800 ns (Figure S5)). Likewise, all trials demonstrate rapid rotation in the range of $\phi = 1.9$ to $\phi = 0.4$ rad, alluding to a steep decline in the rotational free energy landscape. The probability density in Figure 2 is used to track trends across trials, demonstrating multiple semi-stable states in the range of $\phi = 1.9$ to $\phi = 2.6$ rad, as sampled by the three X-Up trials. The persistence of X-Up trial 2 around $\phi = 2.6$ rad for 250 ns and around $\phi = 2.2$ rad for the following 550 ns indicates the presence of multiple semi-stable states along the rotational pathway. To identify these states, the phi data for all runs was fit to a sum of four gaussians, yielding a function with mean values of $\phi = 0.4, 1.9, 2.2, 2.6$ rad, highlighted in Figure 2 by the dashed lines (Figure S6). Panel B and C of Figure 2 feature representative structure for states at $\phi = 2.2$ and $\phi = 0.4$ rad, respectively. At $\phi = 0.4$ rad, the lid is aligned with the interface, adopting an open conformation which exposes the hydrophobic underside to the octane phase and affords access to the active site (Figure S7). At $\phi = 2.2$ rad, as with all states above $\phi = 1.5$ rad, the lid domain remains submerged in the aqueous phase and maintains a closed state, occluding the active site.

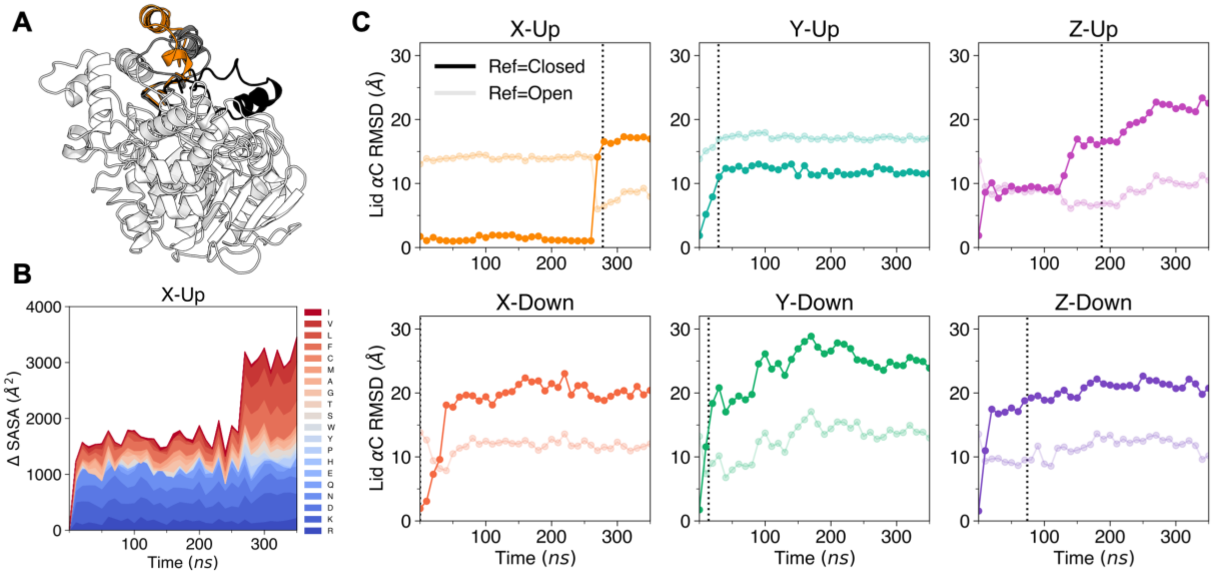

Figure 3. Interfacial Activation is preceded by enzyme rotation at the interface. (a) Representative open lid structure of enzyme CRL is shown for trial X-Up T1 at 350 ns. The lid domain is highlighted in orange and compared to the crystal structure open lid state (gray) and the crystal structure closed lid state (black) All non-lid atoms for the three enzyme structures were aligned to minimize α-carbon RMSD (b) ΔSASA is measured relative to the start frame and grouped by amino acid residue name. Residues are sorted according to theoretical hydropathy index[57] and colored from least hydrophobic (blue) to most hydrophobic (red) (c) Lid domain α-carbon RMSD is calculated relative to the open (light) and closed (dark) crystal structures. The point at which the protein adopts a value of $\phi \leq 0.4$ rad is marked by a dotted black line.

To evaluate lid domain rearrangement in the context of rotation, we measured the RMSD for all lid domain α-carbons (residues 60-97) relative to both the closed and open lid crystal structures over the course of the same 350 ns (Fig 3 panel C). As such, lid opening is interpreted as increasing RMSD relative to the closed state alongside decreasing RMSD relative to the open state. Panel A of Figure 2 shows an example open configuration for X-Up at 350 ns in comparison to the closed (black) and open (gray) lid crystal structures. The accompanying accessibility of the active site is highlighted in Figure S7. For ease of comparison to enzyme orientation, the point in time when the protein adopts an angle $\phi \leq 0.4$ rad is marked by a dotted line in each plot. In the case of X-Down, the lid is facing into the octane phase in the initial state with an angle less than 0.5 rad, therefore the dotted line is marked at 0 ns and lid opening proceeds immediately.

In all cases, lid domain opening begins prior to the cessation of rotation. That is to say that the final orientation of the enzyme is, itself, a function of the lid state. Furthermore, the extent of lid opening is found to be non-uniform between trials. Values for RMSD are expected to vary on account of the flexibility of the lid and are therefore not used as a threshold for lid opening. Rather, the accessibility of the active site is evaluated through a combination of lid domain RMSD and visualization (Figure S7).

All trials, excluding Y-Up, exhibit a crossover event in RMSD values: at this point, the lid more closely aligns with the open state as compared to the closed state. Interestingly, Y-Up exhibits an alternate mode of lid opening where the lid domain folds onto itself and persists to 1 microsecond (Figure S3, S7). Rather than the hydrophilic side of the flap folding back to interact with the non-lid residues on the protein surface, the lid folds onto itself. To evaluate the alternate modes of lid opening observed, we quantified per residue RMSD of lid domain alpha carbons (Figure S8). To note, the lid domain residues in the range of 80-90 for trial Y-Up remain affixed to the protein core, differing from the other trials. These findings prompt further investigation into the alternate modalities of lid opening with consideration of the approach angle to the interface.

While lid opening prompts a loss of common secondary structure relative to the initial closed state, the specific secondary structure of the open state crystallographic reference is not adopted within the simulation time. This indicates that adopting the open state configuration may proceed via a concerted process consisting of lid hinging and structural rearrangement, the latter of which likely requires time scales beyond the scope of classical simulation. As the mechanistic basis of lid domain rearrangement is not presently well understood, additional studies would be required to evaluate the energetics of this rearrangement and the role of the interface. Furthermore, there is an implicit presumption that the open and closed crystal structures represent opposite ends of the interfacial activation pathway. To note, the experimental conditions of the open structure crystallographic study did not include the presence of an oil-water interface. Without proof of this presumption, the diversity of states accessible to the enzyme at the oil-water interface is not necessarily restricted to the conformer preferentially adopted in the crystal form. Within this context, we choose to focus on the accessibility of the active site as evidence of lid domain opening and the stability of the open structure is borne out by the persistence of the lid open state.

The X-Up trials are a standout case in which the lid domain is initially submerged in the aqueous phase. It is important to note that in all trials of this candidate initial orientation, the lid domain exhibits negligible rearrangement prior to contacting the octane phase. This finding is in line with previous studies demonstrating reduced activity in the absence of nonpolar solvent[7]. Importantly, it indicates an initial driving force for rotation outside of the lid domain. It is this effect that we seek to explore in this work.

To gain insight into the driving force behind enzyme rotation and subsequent lid opening, we measured the change in solvent accessible area (SASA) for all residues in contact with the octane phase (within 4Å) referenced to the first frame. Results for all trials are shown in Figure S9 and an example for X-Up trial 1 is shown in panel B of Figure 3. Results are organized by residue type and colored (blue to red) by increasing theoretical hydrophobicity[57]. All trials exhibit an initial increase in total SASA in the first few nanoseconds of simulation due to side chain reorientation at the oil-water interface, having initially been equilibrated in pure water. The next significant change in SASA occurs at the point of lid opening and is largely attributable to Val, Leu, and Phe residues. These results suggest the lid open state is stabilized by the hydrophobic effect, mediated between the octane phase and hydrophobic residues initially on the underside of the lid. The preponderance of aliphatic and aromatic residues has previously been shown to be integral for the recognition and binding of hydrophobic substrates[9]. Transition to the open form results in an increase of the total hydrophobic surface by approximately 1300 $Å^2$ for residues in contact with octane. These results demonstrate an increase in overall surface area with interfacial activation, consistent with previous studies that have measured an increase in hydrophobic surface area of 1300 $Å^2$ upon lid opening.[15]

Collectively, the results of unbiased simulations suggest a minimum in free energy along the rotational landscape that occurs at an angle of approximately 0.4 rad and coincides with a transition in the lid domain from the closed to the open state. While exposure of the hydrophobic underside of the lid to the octane phase provides a driving force for lid opening, enzyme rotation proceeds lid domain rearrangement and as such is mediated by residues outside of the lid domain. These unbiased studies serve to validate the occurrence of interfacial activation at the octane-water interface and provide a basis for which to compare subsequent mutagenesis studies.

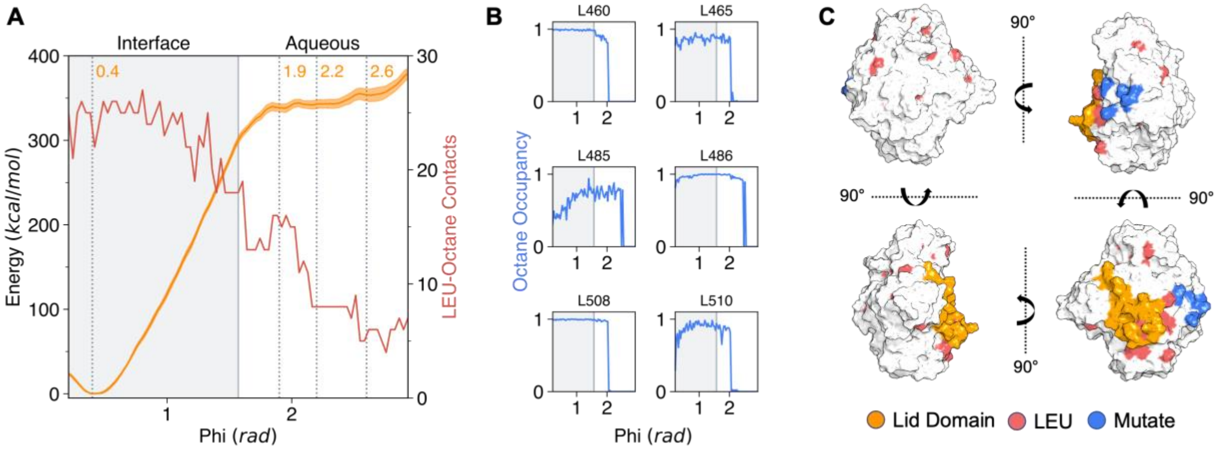

Figure 4. Interfacial activation is accompanied by increasing prevalence of octane-leucine contacts. (a) The free energy of rotation (orange) for enzyme CRL at the oil-water interface was evaluated over a range $\phi = 0.35$ to $\phi = 2.97$ rad. Minima predicted from unbiased simulations are marked by dotted lines at $\phi = 0.4,1.9,2.2,2.6$ rad. Two regions of the simulation, interface and aqueous, are differentiated by the shaded and non-shaded regions, respectively. Interfacial windows exhibit contact (within 4 Å) between the lid domain and the octane phase and in turn demonstrate interfacial activation and lid domain rearrangement. In response, windows within the aqueous region were equilibrated for 25 ns; the interfacial phase, for 40 ns. The average number of Leu residues in contact with the octane phase are evaluated for each window and highlighted in pink (within 4 Å for > 10% of window frames). Contacts for all other residues are included in Figure S10. Octane occupancy (fraction of frames per window within 4 Å of octane) are shown (b) for 6 leucine residues: L460, L465, L485, L486, L508, and L510, and demonstrate contact with the octane phase prior to the lid domain – indicated by the gray shaded region. These six residues are mutated to glycine for subsequent analyses. For clarity, the locations of select residues are differentiated on the enzyme surface (c), including the lid domain (orange), non-mutated leucine residues (pink), and mutated leucine residues (blue).

Umbrella Sampling yields free energy demonstrating quasi-barrier less rotation and global minima following interfacial activation. Based on the results of unbiased simulations, a campaign of Umbrella Sampling simulations was performed to evaluate the free energy of rotation for enzyme CRL about the oil-water interface. In each window, the enzyme was restrained (kappa $= 5{,}000\ \frac{\text{kcal}}{\text{mol}\cdot\text{rad}}$) at a set value of ϕ to the interface while allowing for free rotation within the plane of the interface. After an initial 15 ns of simulations for all 79 frames (the first 5 ns left to equilibration), the number of contacts between octane molecules and lid domain residues (60-97) was evaluated to determine the location of the lid relative to the interface. Windows containing any lid domain residue in contact with the octane phase (i.e., $\leq 4\text{Å}$ for $\geq 10\%$ of frames) were classified as interfacial, all else were classified as aqueous. The cutoff was found to occur at approximately 1.6 rad. To conserve computation resources, longer equilibration was afforded to interfacial windows with the understanding that lid domain rearrangement at the interface would be the most significant constraint on convergence. As anticipated, aqueous phase windows demonstrated convergence in free energy after 15 ns of equilibration, whereas interfacial windows demonstrated convergence after 30 ns (Figure S12). All production frames consisted of 10 ns of sampling per window. For each period of equilibration evaluated we likewise monitored the average lid domain RMSD (referenced to the lid close state). As such, the depression in free energy around $\phi \approx 0.4$ rad with progressive equilibration is shown to be a result of lid domain rearrangement and resulting exposure of hydrophobic residues to the octane phase (Figure S9). For the interfacial category of windows, extending the equilibration from 5 to 40 ns resulted in a decrease in free energy of approximately 100 kcals, unambiguously a result of lid opening (Figure S12).

Final durations of equilibration were 25 ns and 40 ns for aqueous and interfacial frames, respectively. The resulting free energy surface is shown in Figure 4. Predictions of stable states along the rotational pathways based on unbiased simulations ($\phi = 0.4, 1.9, 2.2, 2.6$ rad) are emphasized by dotted lines. The hypothesized semi-stable states are confirmed by three shallow local minima in the anticipated range of phi values and a significantly favorable global minima at $\phi \approx 0.4$ rad. As expected, the transition to lower values of phi is essentially barrier-less as the maximum hurdle along the pathway is on the order of 2 kcal. The ≈ 340 kcal drop in free energy beyond 1.9 radians explains the rapid rotation observed during unbiased runs.

Hydrophobic interactions mediate enzyme rotation prior to lid opening. To probe the driving force behind enzyme rotation and lid domain rearrangement at the interface, we evaluated the nature and number of contacts between the enzyme and the octane phase throughout the course of biased rotation. More specifically, we measured the average number of contacts (≤ 4Å) between octane molecules and CRL residues per residue type in each window (Figure S10). Again, residues are arranged and colored according to the hydropathy index for ease of distinction between hydrophilic and hydrophobic side chains. The most significant change in the number of octane-residue contacts with rotation is observed for leucine residues: from $\phi = 2.6$ to $\phi = 0.4$ rad the number of leucine residues in contact with the octane phase increases from approximately 8 to 28 residues. Leucine contacts for each window are overlaid with free energy in Figure 4 panel A. This is consistent with results from unbiased simulation (Figure S10). It is important to note that while the number of octane-leucine residues increases by approximately 10 residues following lid opening ($\phi > 1.6$ rad), the initial increase by 10 residue contacts occurs during the transition between semi-stable states in the range of $\phi = 1.9$ and $\phi = 2.6$ rad. Within this range of rotation, the lid domain remains submerged in the aqueous phase. Therefore, we hypothesize that these leucine residues facilitate the necessary enzyme rotation to orient the lid at the interface for opening. Lid opening and the subsequent stabilization of the enzyme at the oil-water interface is shown to be mediated by hydrophobic residues on the underside of the lid; however, additional hydrophobic residues are implicated in enzyme rotation prior to lid opening.

While leucine is not the only hydrophobic residue with increasing octane phase contact upon rotation, its effect is most pronounced and as such the residue type was chosen as the focus of this study. To evaluate the impact of leucine residues on the rotational landscape, select leucine residues were mutated to glycine, eliminating the hydrophobic interactions between their side chains and the octane phase. Only leucine residues that are solvent exposed in the closed state and exhibit no lid contact (> 4 Å) were considered for mutation. Additionally, candidates for mutation were required to contact the octane phase prior to any of the lid residues, ensuring that their role in rotation was independent of the lid state. As demonstrated in Figure 4, these criteria were met by 6 leucine residues: L460, L465, L485, L486, L508, and L510. Their location relative to the lid domain is emphasized in panel C of Figure 4 with blue coloring. In the same figure, the location of the lid is differentiated in orange and all other leucine residues in pink. Several leucine surface residues are found at the tip of the lid (near residues 70-80) where initial lid opening is consistently exhibited (Figure S8). Additionally, the blue-shaded leucine residues constitute a hydrophobic patch on the enzyme surface that connects two sides of the enzyme, one containing the lid domain and the other not. Visually, it appears to function as a hydrophobic bridge for rotation towards the global minimum state. We explore the role of this cluster in promoting enzyme rotation via mutagenesis.

Mutant CRL does not exhibit interfacial activation on the order of 1 microsecond. Following the same protocol for initialization, equilibration, and production as with the native enzyme, three trials of mutant enzymes were run for three distinct random packings of the enzyme initialized in the X-Up configuration. To note, in this configuration the lid is initially submerged in the aqueous phase. Based on the observation from native simulations that the limiting step of interfacial activation was rotation and alignment of the lid domain with the interface, only the X-Up starting configuration was evaluated for mutant runs. Likewise, frames spanning the range of $\phi = 0.35$ to $\phi = 2.97$ rad were sought for consistency with native protein umbrella sampling. Enzyme stability following mutation was confirmed through negligible non-lid α-carbons RMSD over the course of simulation (Figure S14). After extending all 3 trials to 1 microsecond, none of the runs showed rotation beyond $\phi = 2.2$ radians (Figure S15). While this indicates an imposed barrier to rotation, it precludes access to frames at lower values of phi required for Umbrella Sampling. Therefore, steering was performed to pull the enzyme between 2.1 and 1.3 radians. Next, frames were selected from the steered trajectory to be used as starting states for unbiased runs. Resulting orientations are showcased in Figure S17. While trajectories beginning from $\phi = 1.7, 1.8$ demonstrate return to $\phi \approx 2.2$ radians, those beginning from $\phi = 1.6, 1.65$ exhibit continued rotation to $\phi \approx 0.4$ radians. Based on this finding, the barrier introduced through mutation is anticipated to appear in the range of 1.6 to 1.7 radians.

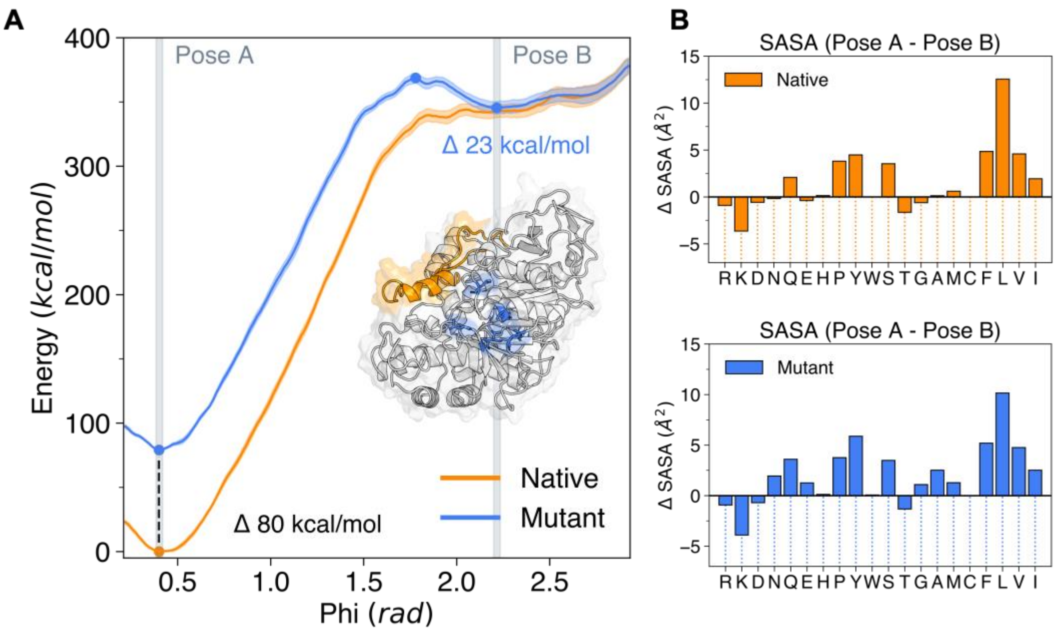

Figure 5. The rotational landscape for native versus mutant CRL. (a) The free energy of rotation for native (orange) and mutant (blue) CRL are compared. A barrier to rotation of approximately 23 kcals/mol is shown for traversal of the mutant enzyme to lower values of ϕ, including the global minimum at $\phi \approx 0.4$ rad. While the global minimum in free energy is conserved between the native and mutant enzymes, the native enzyme demonstrates a greater delta between its highest and lowest energy states of approximately 80 kcals/mol compared to the mutant enzyme over the same range of ϕ values. Two angles relative to the interface, pose A (0.4 rad) and pose B (2.2 rad), are emphasized by shading. (b) The corresponding per residue ΔSASA for octane-contacting residues are displayed in panel B with values at pose B subtracted from those at pose A. Results for the native protein are shown in orange and the mutant in blue. Residue names are sorted according to increasing theoretical hydrophobicity to highlight the trend in residue-octane contacts: at the lesser angle to the interface (pose A and following interfacial activation) there is greater contact area between octane and hydrophobic residues and lesser contact area between octane and hydrophilic residues.

Mutation to LEU residues outside of the lid domain imposes a barrier to rotation. Figure 5 panel A compares the free energy surfaces as a function of phi for both the native and mutant enzymes. Plots are aligned to the highest energy value, occurring at $\phi \approx 2.9$ rad. Two local minima of the mutant rotation occur at $\phi \approx 2.3, 2.6$ rad, consistent with sampling observed in classical simulations. Whereas the native protein experiences an essentially barrier-less rotation, the mutant enzyme must surmount a ≈ 23 kcal/mol barrier at approximately 1.6 radians to rotate from the global maximum to the global minimum. This explains the lack of rotation in mutant classical simulations out to 1 microsecond. Viewing the mutated residues (highlighted in blue in Figure 4 panel B), we observe that they lie directly on the rotational pathway between local and global minima, serving as a hydrophobic bridge between the states. Therefore, it is posited that these residues, despite being located outside of the lid domain and active site, play an important role in aligning the enzyme for activity at the oil-water interface.

Despite introducing a barrier to rotation, mutation does not alter the location of the lowest free energy state, consistently observed at $\phi \approx 0.4$ radians. However, the difference in energy between the highest ($\phi = 2.9$) and lowest ($\phi = 0.4$) energy states differ between the two rounds of Umbrella Sampling. This can be explained by the difference in contacts between the octane phase and the enzyme at the lowest energy state following mutation. Namely, six interactions between octane and the hydrophobic side chains of leucine are eliminated in the mutant enzyme. To evaluate this effect, a set of Umbrella Sampling simulations were run where capped (ACE, NME) amino acids of either leucine or glycine were pulled through an octane-water interface. Next, the $\Delta\Delta G$ for the transition from water to octane between leucine and glycine was estimated to be approximately 19 kcal (Figure S21). For six residues mutated, this places a maximum estimate for $\Delta\Delta G$ on the order of 114 kcal. Considering the corresponding amino acids in the whole enzyme simulations are solvent exposed to a lesser degree, it is expected that the measured value of $\Delta\Delta G$ would be less than the 114 kcal estimate. As such, the actual measured value of 80 kcal is in line with expectation.

To explain the significant decline in free energy with rotation, we compared two poses at $\phi \approx 0.4$ rad (Pose A) and $\phi \approx 2.2$ rad (Pose B). The average solvent accessible surface of amino acids in contact with the octane phase was evaluated for both poses. Resulting values for Pose B were subtracted from Pose A, highlighting the interactions introduced following rotation and lid domain opening (Figure 5 Panel B). Once again, amino acids are sorted according to the hydropathy index for visualization. For the native and mutant enzymes, there is a loss of contacts between octane and the most hydrophilic residues (Arg, Lys, Asp) and an increase in contacts between octane and the most hydrophobic residues (Ile, Leu, Val, Phe). These changes explain the difference in free energy and provide a driving force for lid opening and rotation. As is expected the extent of octane-leucine contact is decreased between the native and mutant enzymes.

Conclusion

Here, we have evaluated the solvent interactions and energetics of interfacial activation for enzyme CRL at the octane-water interface. In particular, we have demonstrated consistent lid opening beginning from a diversity of initial states. Through classical and biased Molecular Dynamics simulations we probed the effect of lid opening on octane-amino acid interactions and in turn, the role of octane-amino acid interactions in instigating lid domain opening. While lid opening, with accompanying hydrophobic interactions between the octane phase and the underside of the lid domain, is shown to stabilize the lid open conformation and defines the final orientation of the enzyme, rotation at the oil-water interface is shown to be initially instigated by hydrophobic residues outside of the lid domain, namely a cluster of leucine residues that bridge the two stable interfacial states of the enzyme. This is not to present the selected mutated residues as exhaustive of the hydrophobic residues that play a role in the rotational dynamics of the enzyme. Rather, the mutations at these residues are merely sufficient to impose a barrier to rotation and indicate a cooperative effect between the lid domain and tangential hydrophobic residues for facilitating the process of lid opening. Given the ubiquitous nature of lid domains among lipases, there are abundant opportunities for continued exploration into the holistic effects of enzyme surface residues on rotation at oil-water interfaces for other lipases.

Additionally, future work should investigate the mechanism of lid opening at the oil water interface, namely the rearrangement of lid secondary structure required for the transition between lid closed and open states as observed in the x-ray crystal structures.

References

1. Gotor-Fernández, V.; Brieva, R.; Gotor, V. Lipases: Useful Biocatalysts for the Preparation of Pharmaceuticals. J. Mol. Catal. B Enzym. **2006**, 40 (3), 111–120. https://doi.org/10.1016/j.molcatb.2006.02.010.
2. Tan, T.; Lu, J.; Nie, K.; Deng, L.; Wang, F. Biodiesel Production with Immobilized Lipase: A Review. Biotechnol. Adv. **2010**, 28 (5), 628–634. https://doi.org/10.1016/j.biotechadv.2010.05.012.
3. Enzymatic Polymer Synthesis: An Opportunity for Green Polymer Chemistry | Chemical Reviews. https://pubs-acs-org.offcampus.lib.washington.edu/doi/full/10.1021/cr900165z.
4. Mehta, A.; Guleria, S.; Sharma, R.; Gupta, R. 6 - The Lipases and Their Applications with Emphasis on Food Industry. In Microbial Biotechnology in Food and Health; Ray, R. C., Ed.; Applied Biotechnology Reviews; Academic Press, 2021; pp 143–164. https://doi.org/10.1016/B978-0-12-819813-1.00006-2.
5. Industrial applications of microbial lipases - ScienceDirect. https://www-sciencedirect-com.offcampus.lib.washington.edu/science/article/abs/pii/S0141022905004606.
6. Colton, I. J.; Ahmed, S. N.; Kazlauskas, R. J. A 2-Propanol Treatment Increases the Enantioselectivity of Candida Rugosa Lipase toward Esters of Chiral Carboxylic Acids. J. Org. Chem. **1995**, 60 (1), 212–217. https://doi.org/10.1021/jo00106a036.
7. Chamorro, S.; Sánchez-Montero, J. M.; Alcántara, A. R.; Sinisterra, J. V. Treatment of Candida Rugosa Lipase with Short-Chain Polar Organic Solvents Enhances Its Hydrolytic and Synthetic Activities. Biotechnol. Lett. **1998**, 20 (5), 499–505. https://doi.org/10.1023/A:1005448431237.
8. Tejo, B. A.; Salleh, A. B.; Pleiss, J. Structure and Dynamics of Candida Rugosa Lipase: The Role of Organic Solvent. J. Mol. Model. **2004**, 10 (5), 358–366. https://doi.org/10.1007/s00894-004-0203-z.
9. Lipases at interfaces: A review - ScienceDirect. https://www-sciencedirect-com.offcampus.lib.washington.edu/science/article/abs/pii/S0001868608001000.
10. Arana-Peña, S.; Rios, N. S.; Carballares, D.; Gonçalves, L. R. B.; Fernandez-Lafuente, R. Immobilization of Lipases via Interfacial Activation on Hydrophobic Supports: Production of Biocatalysts Libraries by Altering the Immobilization Conditions. Catal. Today **2021**, 362, 130–140. https://doi.org/10.1016/j.cattod.2020.03.059.
11. Zhang, J.; Wang, Z.; Zhuang, W.; Rabiee, H.; Zhu, C.; Deng, J.; Ge, L.; Ying, H. Amphiphilic Nanointerface: Inducing the Interfacial Activation for Lipase. ACS Appl. Mater. Interfaces **2022**, 14 (34), 39622–39636. https://doi.org/10.1021/acsami.2c11500.
12. Rodrigues, R. C.; Virgen-Ortíz, J. J.; dos Santos, J. C. S.; Berenguer-Murcia, Á.; Alcantara, A. R.; Barbosa, O.; Ortiz, C.; Fernandez-Lafuente, R. Immobilization of Lipases on Hydrophobic Supports: Immobilization Mechanism, Advantages, Problems, and Solutions. Biotechnol. Adv. **2019**, 37 (5), 746–770. https://doi.org/10.1016/j.biotechadv.2019.04.003.
13. Grochulski, P.; Li, Y.; Schrag, J. D.; Bouthillier, F.; Smith, P.; Harrison, D.; Rubin, B.; Cygler, M. Insights into Interfacial Activation from an Open Structure of Candida Rugosa Lipase. J. Biol. Chem. **1993**, 268 (17), 12843–12847. https://doi.org/10.1016/S0021-9258(18)31464-9.
14. Mancheño, J. M.; Pernas, M. A.; Martínez, M. J.; Ochoa, B.; Rúa, M. L.; Hermoso, J. A. Structural Insights into the Lipase/Esterase Behavior in the Candida Rugosa Lipases

Family: Crystal Structure of the Lipase 2 Isoenzyme at 1.97 Å Resolution. J. Mol. Biol. **2003**, 332 (5), 1059–1069. https://doi.org/10.1016/j.jmb.2003.08.005.

15. Structure and conformational flexibility of Candida rugosa lipase - ScienceDirect. https://www-sciencedirect-com.offcampus.lib.washington.edu/science/article/pii/S1388198199001523.
16. Grochulski, P.; Li, Y.; Schrag, J. D.; Cygler, M. Two Conformational States of Candida Rugosa Lipase. Protein Sci. **1994**, 3 (1), 82–91. https://doi.org/10.1002/pro.5560030111.
17. Barriuso, J.; Vaquero, M. E.; Prieto, A.; Martínez, M. J. Structural Traits and Catalytic Versatility of the Lipases from the Candida Rugosa-like Family: A Review. Biotechnol. Adv. **2016**, 34 (5), 874–885. https://doi.org/10.1016/j.biotechadv.2016.05.004.
18. Pernas, M. A.; Pastrana, L.; Fuciños, P.; Rúa, M. L. Regulation of the Interfacial Activation within the Candida Rugosa Lipase Family. J. Phys. Org. Chem. **2009**, 22 (5), 508–514. https://doi.org/10.1002/poc.1513.
19. López, N.; Pernas, M. A.; Pastrana, L. M.; Sánchez, A.; Valero, F.; Rúa, M. L. Reactivity of Pure Candida Rugosa Lipase Isoenzymes (Lip1, Lip2, and Lip3) in Aqueous and Organic Media. Influence of the Isoenzymatic Profile on the Lipase Performance in Organic Media. Biotechnol. Prog. **2004**, 20 (1), 65–73. https://doi.org/10.1021/bp034188c.
20. Palomo, J. M.; Fernandez-Lorente, G.; Mateo, C.; Ortiz, C.; Fernandez-Lafuente, R.; Guisan, J. M. Modulation of the Enantioselectivity of Lipases via Controlled Immobilization and Medium Engineering: Hydrolytic Resolution of Mandelic Acid Esters. Enzyme Microb. Technol. **2002**, 31 (6), 775–783. https://doi.org/10.1016/S0141-0229(02)00169-2.
21. Sánchez-Morán, H.; Weltz, J. S.; Schwartz, D. K.; Kaar, J. L. Understanding Design Rules for Optimizing the Interface between Immobilized Enzymes and Random Copolymer Brushes. ACS Appl. Mater. Interfaces **2021**, 13 (23), 26694–26703. https://doi.org/10.1021/acsami.1c02443.
22. C-Terminal Region of Candida rugosa Lipases Affects Enzyme Activity and Interfacial Activation | Journal of Agricultural and Food Chemistry. https://pubs-acs-org.offcampus.lib.washington.edu/doi/full/10.1021/jf104721a (accessed 2024-03-10).
23. Lee, L.-C.; Chen, Y.-T.; Yen, C.-C.; Chiang, T. C.-Y.; Tang, S.-J.; Lee, G.-C.; Shaw, J.-F. Altering the Substrate Specificity of Candida Rugosa LIP4 by Engineering the Substrate-Binding Sites. J. Agric. Food Chem. **2007**, 55 (13), 5103–5108. https://doi.org/10.1021/jf0702949.
24. Gutiérrez-Fernández, J.; Vaquero, M. E.; Prieto, A.; Barriuso, J.; Martínez, M. J.; Hermoso, J. A. Crystal Structures of Ophiostoma Piceae Sterol Esterase: Structural Insights into Activation Mechanism and Product Release. J. Struct. Biol. **2014**, 187 (3), 215–222. https://doi.org/10.1016/j.jsb.2014.07.007.
25. Akoh, C. C.; Lee, G.-C.; Shaw, J.-F. Protein Engineering and Applications of Candida Rugosa Lipase Isoforms. Lipids **2004**, 39 (6), 513–526. https://doi.org/10.1007/s11745-004-1258-7.
26. Zisis, T.; Freddolino, P. L.; Turunen, P.; van Teeseling, M. C. F.; Rowan, A. E.; Blank, K. G. Interfacial Activation of Candida Antarctica Lipase B: Combined Evidence from Experiment and Simulation. Biochemistry **2015**, 54 (38), 5969–5979. https://doi.org/10.1021/acs.biochem.5b00586.

27. Structural and Dynamic Features of Candida rugosa Lipase 1 in Water, Octane, Toluene, and Ionic Liquids BMIM-PF6 and BMIM-NO3 | The Journal of Physical Chemistry B. https://pubs-acs-org.offcampus.lib.washington.edu/doi/full/10.1021/jp312299d.
28. Maldonado, M. R.; Alnoch, R. C.; de Almeida, J. M.; Santos, L. A. dos; Andretta, A. T.; Ropaín, R. del P. C.; de Souza, E. M.; Mitchell, D. A.; Krieger, N. Key Mutation Sites for Improvement of the Enantioselectivity of Lipases through Protein Engineering. Biochem. Eng. J. **2021**, 172, 108047. https://doi.org/10.1016/j.bej.2021.108047.
29. Kamal, M. Z.; Mohammad, T. A. S.; Krishnamoorthy, G.; Rao, N. M. Role of Active Site Rigidity in Activity: MD Simulation and Fluorescence Study on a Lipase Mutant. PLOS ONE **2012**, 7 (4), e35188. https://doi.org/10.1371/journal.pone.0035188.
30. Qin, X.; Zhong, J.; Wang, Y. A Mutant T1 Lipase Homology Modeling, and Its Molecular Docking and Molecular Dynamics Simulation with Fatty Acids. J. Biotechnol. **2021**, 337, 24–34. https://doi.org/10.1016/j.jbiotec.2021.06.024.
31. D.A. Case, H.M. Aktulga, K. Belfon, I.Y. Ben-Shalom, J.T. Berryman, S.R. Brozell, D.S. Cerutti, T.E. Cheatham, III, G.A. Cisneros, V.W.D. Cruzeiro, T.A. Darden, N. Forouzesh, G. Giambaşu, T. Giese, M.K. Gilson, H. Gohlke, A.W. Goetz, J. Harris, S. Izadi, S.A. Izmailov, K. Kasavajhala, M.C. Kaymak, E. King, A. Kovalenko, T. Kurtzman, T.S. Lee, P. Li, C. Lin, J. Liu, T. Luchko, R. Luo, M. Machado, V. Man, M. Manathunga, K.M. Merz, Y. Miao, O. Mikhailovskii, G. Monard, H. Nguyen, K.A. O'Hearn, A. Onufriev, F. Pan, S. Pantano, R. Qi, A. Rahnamoun, D.R. Roe, A. Roitberg, C. Sagui, S. Schott-Verdugo, A. Shajan, J. Shen, C.L. Simmerling, N.R. Skrynnikov, J. Smith, J. Swails, R.C. Walker, J. Wang, J. Wang, H. Wei, X. Wu, Y. Wu, Y. Xiong, Y. Xue, D.M. York, S. Zhao, Q. Zhu, and P.A. Kollman (2023), Amber 2023, University of California, San Francisco.
32. D.A. Case, H.M. Aktulga, K. Belfon, D.S. Cerutti, G.A. Cisneros, V.W.D. Cruz Eiro, N. Forouzesh, T.J. Giese, A.W. Götz, H. Gohlke, S. Izadi, K. Kasavajhala, M.C. Kaymak, E. King, T. Kurtzman, T.-S. Lee, P. Li, J. Liu, T. Luchko, R. Luo, M. Manathunga, M.R. Machado, H.M. Nguyen, K.A. O'Hearn, A.V. Onufriev, F. Pan, S. Pantano, R. Qi, A. Rahnamoun, A. Risheh, S. Schott-Verdugo, A. Shajan, J. Swails, J. Wang, H. Wei, X. Wu, Y. Wu, S. Zhang, S. Zhao, Q. Zhu, T.E. Cheatham III, D.R. Roe, A. Roitberg, C. Simmerling, D.M. York, M.C. Nagan*, and K.M. Merz Jr.* AmberTools. J. Chem. Inf. Model. 63, 6183-6191 (2023).
33. ff19SB: Amino-Acid-Specific Protein Backbone Parameters Trained against Quantum Mechanics Energy Surfaces in Solution | Journal of Chemical Theory and Computation. https://pubs-acs-org.offcampus.lib.washington.edu/doi/full/10.1021/acs.jctc.9b00591.
34. Izadi, S.; Anandakrishnan, R.; Onufriev, A. V. Building Water Models: A Different Approach. J. Phys. Chem. Lett. **2014**, 5 (21), 3863–3871. https://doi.org/10.1021/jz501780a.
35. Development and testing of a general amber force field - Wang - 2004 - Journal of Computational Chemistry - Wiley Online Library. https://onlinelibrary-wiley-com.offcampus.lib.washington.edu/doi/abs/10.1002/jcc.20035
36. Parameterization of Monovalent Ions for the OPC3, OPC, TIP3P-FB, and TIP4P-FB Water Models | Journal of Chemical Information and Modeling. https://pubs-acs-org.offcampus.lib.washington.edu/doi/full/10.1021/acs.jcim.0c01390.
37. Bayly, C. I.; Cieplak, P.; Cornell, W.; Kollman, P. A. A Well-Behaved Electrostatic Potential Based Method Using Charge Restraints for Deriving Atomic Charges: The

RESP Model. J. Phys. Chem. **1993**, 97 (40), 10269–10280. https://doi.org/10.1021/j100142a004.

38. Gaussian 16, Revision C.01, Frisch, M. J.; Trucks, G. W.; Schlegel, H. B.; Scuseria, G. E.; Robb, M. A.; Cheeseman, J. R.; Scalmani, G.; Barone, V.; Petersson, G. A.; Nakatsuji, H.; Li, X.; Caricato, M.; Marenich, A. V.; Bloino, J.; Janesko, B. G.; Gomperts, R.; Mennucci, B.; Hratchian, H. P.; Ortiz, J. V.; Izmaylov, A. F.; Sonnenberg, J. L.; Williams-Young, D.; Ding, F.; Lipparini, F.; Egidi, F.; Goings, J.; Peng, B.; Petrone, A.; Henderson, T.; Ranasinghe, D.; Zakrzewski, V. G.; Gao, J.; Rega, N.; Zheng, G.; Liang, W.; Hada, M.; Ehara, M.; Toyota, K.; Fukuda, R.; Hasegawa, J.; Ishida, M.; Nakajima, T.; Honda, Y.; Kitao, O.; Nakai, H.; Vreven, T.; Throssell, K.; Montgomery, J. A., Jr.; Peralta, J. E.; Ogliaro, F.; Bearpark, M. J.; Heyd, J. J.; Brothers, E. N.; Kudin, K. N.; Staroverov, V. N.; Keith, T. A.; Kobayashi, R.; Normand, J.; Raghavachari, K.; Rendell, A. P.; Burant, J. C.; Iyengar, S. S.; Tomasi, J.; Cossi, M.; Millam, J. M.; Klene, M.; Adamo, C.; Cammi, R.; Ochterski, J. W.; Martin, R. L.; Morokuma, K.; Farkas, O.; Foresman, J. B.; Fox, D. J. Gaussian, Inc., Wallingford CT, 2016.
39. Kräutler, V.; van Gunsteren, W. F.; Hünenberger, P. H. A Fast SHAKE Algorithm to Solve Distance Constraint Equations for Small Molecules in Molecular Dynamics Simulations. J. Comput. Chem. **2001**, 22 (5), 501–508. https://doi.org/10.1002/1096-987X(20010415)22:5<501::AID-JCC1021>3.0.CO;2-V.
40. Miyamoto, S.; Kollman, P. A. Settle: An Analytical Version of the SHAKE and RATTLE Algorithm for Rigid Water Models. J. Comput. Chem. **1992**, 13 (8), 952–962. https://doi.org/10.1002/jcc.540130805.
41. Long-Time-Step Molecular Dynamics through Hydrogen Mass Repartitioning | Journal of Chemical Theory and Computation. https://pubs-acs-org.offcampus.lib.washington.edu/doi/full/10.1021/ct5010406.
42. Darden, T.; York, D.; Pedersen, L. Particle Mesh Ewald: An N·log(N) Method for Ewald Sums in Large Systems. J. Chem. Phys. **1993**, 98 (12), 10089–10092. https://doi.org/10.1063/1.464397.
43. Bussi, G.; Donadio, D.; Parrinello, M. Canonical Sampling through Velocity Rescaling. J. Chem. Phys. **2007**, 126 (1), 014101. https://doi.org/10.1063/1.2408420.
44. Berendsen, H. J. C.; Postma, J. P. M.; van Gunsteren, W. F.; DiNola, A.; Haak, J. R. Molecular Dynamics with Coupling to an External Bath. J. Chem. Phys. **1984**, 81 (8), 3684–3690. https://doi.org/10.1063/1.448118.
45. Åqvist, J.; Wennerström, P.; Nervall, M.; Bjelic, S.; Brandsdal, B. O. Molecular Dynamics Simulations of Water and Biomolecules with a Monte Carlo Constant Pressure Algorithm. Chem. Phys. Lett. **2004**, 384 (4), 288–294. https://doi.org/10.1016/j.cplett.2003.12.039.
46. Gordon, J. C.; Myers, J. B.; Folta, T.; Shoja, V.; Heath, L. S.; Onufriev, A. H++: A Server for Estimating pKas and Adding Missing Hydrogens to Macromolecules. Nucleic Acids Res. **2005**, 33 (Web Server issue), W368–W371. https://doi.org/10.1093/nar/gki464.
47. Humphrey, W., Dalke, A. and Schulten, K., “VMD - Visual Molecular Dynamics”, J. Molec. Graphics, 1996, Vol. 14, Pp. 33-38.

48. Martínez, L.; Andrade, R.; Birgin, E. G.; Martínez, J. M. PACKMOL: A package for building initial configurations for molecular dynamics simulations. J. Comput. Chem. **2009**, 30 (13), 2157–2164. https://doi.org/10.1002/jcc.21224.
49. Bonomi, M.; Branduardi, D.; Bussi, G.; Camilloni, C.; Provasi, D.; Raiteri, P.; Donadio, D.; Marinelli, F.; Pietrucci, F.; Broglia, R. A.; Parrinello, M. PLUMED: A Portable Plugin for Free-Energy Calculations with Molecular Dynamics. Comput. Phys. Commun. **2009**, 180 (10), 1961–1972. https://doi.org/10.1016/j.cpc.2009.05.011.
50. Tribello, G. A.; Bonomi, M.; Branduardi, D.; Camilloni, C.; Bussi, G. PLUMED 2: New Feathers for an Old Bird. Comput. Phys. Commun. **2014**, 185 (2), 604–613. https://doi.org/10.1016/j.cpc.2013.09.018.
51. Bonomi, M.; Bussi, G.; Camilloni, C.; Tribello, G. A.; Banáš, P.; Barducci, A.; Bernetti, M.; Bolhuis, P. G.; Bottaro, S.; Branduardi, D.; Capelli, R.; Carloni, P.; Ceriotti, M.; Cesari, A.; Chen, H.; Chen, W.; Colizzi, F.; De, S.; De La Pierre, M.; Donadio, D.; Drobot, V.; Ensing, B.; Ferguson, A. L.; Filizola, M.; Fraser, J. S.; Fu, H.; Gasparotto, P.; Gervasio, F. L.; Giberti, F.; Gil-Ley, A.; Giorgino, T.; Heller, G. T.; Hocky, G. M.; Iannuzzi, M.; Invernizzi, M.; Jelfs, K. E.; Jussupow, A.; Kirilin, E.; Laio, A.; Limongelli, V.; Lindorff-Larsen, K.; Löhr, T.; Marinelli, F.; Martin-Samos, L.; Masetti, M.; Meyer, R.; Michaelides, A.; Molteni, C.; Morishita, T.; Nava, M.; Paissoni, C.; Papaleo, E.; Parrinello, M.; Pfaendtner, J.; Piaggi, P.; Piccini, G.; Pietropaolo, A.; Pietrucci, F.; Pipolo, S.; Provasi, D.; Quigley, D.; Raiteri, P.; Raniolo, S.; Rydzewski, J.; Salvalaglio, M.; Sosso, G. C.; Spiwok, V.; Šponer, J.; Swenson, D. W. H.; Tiwary, P.; Valsson, O.; Vendruscolo, M.; Voth, G. A.; White, A.; The PLUMED consortium. Promoting Transparency and Reproducibility in Enhanced Molecular Simulations. Nat. Methods **2019**, 16 (8), 670–673. https://doi.org/10.1038/s41592-019-0506-8.
52. Grossfield, Alan, "WHAM: The Weighted Histogram Analysis Method", Version 2.0.11, Http://Membrane.Urmc.Rochester.Edu/Wordpress/?Page_id=126.
53. Michaud-Agrawal, N.; Denning, E. J.; Woolf, T. B.; Beckstein, O. MDAnalysis: A Toolkit for the Analysis of Molecular Dynamics Simulations. J. Comput. Chem. **2011**, 32 (10), 2319–2327. https://doi.org/10.1002/jcc.21787.
54. Gowers, R.; Linke, M.; Barnoud, J.; Reddy, T.; Melo, M.; Seyler, S.; Domański, J.; Dotson, D.; Buchoux, S.; Kenney, I.; Beckstein, O. MDAnalysis: A Python Package for the Rapid Analysis of Molecular Dynamics Simulations; Austin, Texas, 2016; pp 98–105. https://doi.org/10.25080/Majora-629e541a-00e.
55. McGibbon, R. T.; Beauchamp, K. A.; Harrigan, M. P.; Klein, C.; Swails, J. M.; Hernández, C. X.; Schwantes, C. R.; Wang, L.-P.; Lane, T. J.; Pande, V. S. MDTraj: A Modern Open Library for the Analysis of Molecular Dynamics Trajectories. Biophys. J. **2015**, 109 (8), 1528–1532. https://doi.org/10.1016/j.bpj.2015.08.015.
56. Schrödinger, LLC. The PyMOL Molecular Graphics System, Version 1.8, 2015.
57. Kyte, J.; Doolittle, R. F. A Simple Method for Displaying the Hydropathic Character of a Protein. J. Mol. Biol. **1982**, 157 (1), 105–132. https://doi.org/10.1016/0022-2836(82)90515-0.